

## Modeling the transport and radiative forcing of Taklimakan dust over the Tibetan Plateau: A case study in the summer of 2006

Siyu Chen,<sup>1,2</sup> Jianping Huang,<sup>1</sup> Chun Zhao,<sup>2</sup> Yun Qian,<sup>2</sup> L. Ruby Leung,<sup>2</sup> and Ben Yang<sup>2,3</sup>

Received 10 July 2012; revised 11 December 2012; accepted 17 December 2012.

[1] The Weather Research and Forecasting model with chemistry (WRF-Chem) is used to investigate an intense dust storm event during 26 to 30 July 2006 that originated over the Taklimakan Desert (TD) and transported to the northern slope of Tibetan Plateau (TP). The dust storm is initiated by the approach of a strong cold frontal system over the TD. In summer, the meridional transport of TD dust to the TP is favored by the thermal effect of the TP and the weakening of the East Asian westerly winds. During this dust storm, the transport of TD dust over the TP is further enhanced by the passage of the cold front. As a result, TD dust breaks through the planetary boundary layer and extends to the upper troposphere over the northern TP. TD dust flux arrived at the TP with a value of 6.6 Gg/day in this 5 day event but decays quickly during the southward migration over the TP due to dry deposition. The simulations show that TD dust cools the atmosphere near the surface and heats the atmosphere above with a maximum heating rate of 0.11 K day<sup>-1</sup> at ~7 km over the TP. The event-averaged net radiative forcings of TD dust over the TP are -3.97, 1.61, and -5.58 W m<sup>-2</sup> at the top of the atmosphere (TOA), in the atmosphere, and at the surface, respectively. The promising performance of WRF-Chem in simulating dust and its radiative forcing provides confidence for use in further investigation of climatic impact of TD dust over the TP.

**Citation:** Chen, S., J. Huang, C. Zhao, Y. Qian, L. R. Leung, and B. Yang (2013), Modeling the transport and radiative forcing of Taklimakan dust over the Tibetan Plateau: A case study in the summer of 2006, *J. Geophys. Res. Atmos.*, 118, doi:10.1002/jgrd.50122.

### 1. Introduction

[2] Dust is one of the most important aerosol species in the atmosphere because it has the largest abundance of mass compared to other aerosols [Forster *et al.*, 2007]. Dust can affect the atmospheric system and energy budget by scattering and absorbing shortwave and longwave radiation (i.e., “direct effect”) [Ramanathan *et al.*, 2001; Huang *et al.*, 2009; Lau *et al.*, 2009; Zhao *et al.*, 2010, 2011, 2012] and modifying the microphysical properties of clouds (i.e., “indirect effects” and “semi-direct effects”) [Twomey *et al.*, 1984; Koren *et al.*, 2004; Huang *et al.*, 2006a,b, 2010; Su *et al.*, 2008; Qian *et al.*, 2009; Wang *et al.*, 2010]. The Taklimakan Desert (TD), one of the largest deserts in the world, is a major dust source region in Asia [Wang *et al.*, 2008]. It covers an area of 337,000 km<sup>2</sup>, bounded by the Kunlun Mountains to the south and the desert Pamir Mountains and Tian Shan to the west and

north (Figure 1). TD dust is thought to have significant climatic impacts, especially at the regional scale [Gautam *et al.*, 2009; Kuhlmann and Quaas, 2010; Huang *et al.*, 2010; Li *et al.*, 2011; Sekiyama *et al.*, 2011; Shao *et al.*, 2011; Liu *et al.*, 2011].

[3] The TD is located in the midlatitude where the East Asian westerly winds prevail. Many studies have focused on the long-range eastward transport of TD dust during spring and summer, when TD dust has the most significant impact on the global dust loading through the year [e.g., Murayama *et al.*, 2001; Uno *et al.*, 2004; Huang *et al.*, 2008; Yumimoto *et al.*, 2009, 2010]. For example, Huang *et al.* [2008] indicated that nonspherical aerosols lifted to an altitude of 9 km around the Asian dust source region could be transported over a long range through the upper troposphere where dust has a relatively longer lifetime. Yumimoto *et al.* [2009] showed that the dust particles from the dust storm during 19–20 May 2007 over the TD were transported intercontinentally over Eastern Asia, the Pacific Ocean, North America, and the Atlantic Ocean. Yumimoto *et al.* [2010] suggested that TD dust was transported across the Pacific Ocean in 12–13 days in summer based on the ground-based lidar networks.

[4] So far, very few studies investigated the transport of TD dust over the Tibetan Plateau (TP) in summer, when the East Asian westerly jet shifts northward and becomes weaker. The East Asian westerly jet is a narrow and strong westerly belt with large horizontal and vertical wind shears over the subtropical East Asia in the upper troposphere and

<sup>1</sup>Key Laboratory for Semi-Arid Climate Change of the Ministry of Education, Lanzhou University, Lanzhou, Gansu, China.

<sup>2</sup>Atmospheric Science and Global Change Division, Pacific Northwest National Laboratory, Richland, WA, USA.

<sup>3</sup>School of Atmospheric Sciences, Nanjing University, Nanjing, China.

Corresponding author: Siyu Chen, Key Laboratory for Semi-Arid Climate Change of the Ministry of Education, Lanzhou University, Lanzhou, Gansu, China. (siyuchen.lzu@gmail.com; siyu.chen@pnnl.gov)

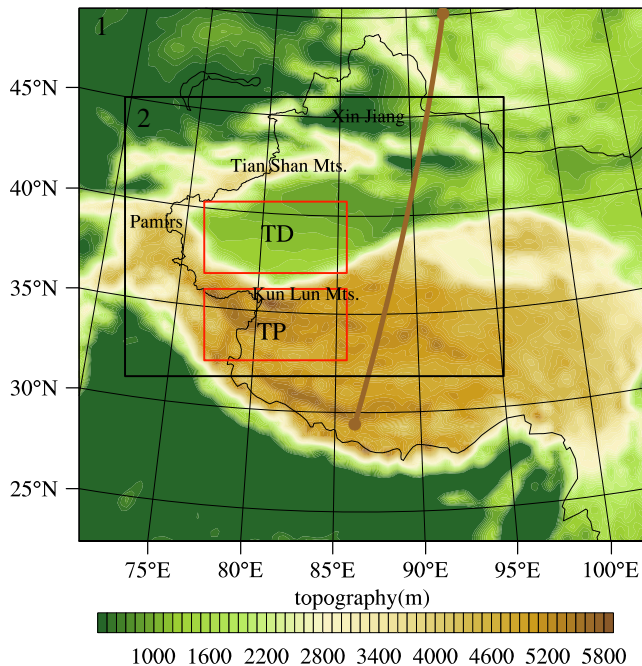


**Figure 1.** Modeling domains and the spatial distribution of topography over the vicinity of TP. Simulations are conducted for domains 1 and 2. The two boxes are defined as the TD (Taklimakan Desert) and TP (Tibetan Plateau) regions for further analysis.

lower stratosphere (about 10–16 km) [Zhang *et al.*, 2008]. The TP extends over a latitude–longitude region of 25–45°N, 70–105°E, with a size of about one quarter of the Chinese territory and a mean elevation of more than 4000 m above the mean sea level (amsl). Therefore, it can significantly influence the atmospheric circulation, energy budget, and hydrological cycles in Asia or even the globe through the dynamical and thermal effect due to its particular orography and large extension [e.g., Ye and Wu, 1998; Wu and Zhang, 1998, 2007]. The TP impacts on regional and global climate could be modified by the dust over the TP. Lau *et al.* [2006] pointed out that the air over the southern slope of the TP can be heated by the dust transported from nearby deserts in northern India during late spring and early summer, which may lead to an earlier onset and intensification of the Indian summer monsoon. Lau *et al.* [2010] showed that atmospheric heating by dust and black carbon can lead to a reduction of snowpack cover by 6%–10% over the western TP and Himalayan regions. In addition, Qian *et al.* [2011] suggested that the changes of surface albedo and radiative fluxes over the TP induced by the deposition of dust and black carbon on the snow of TP could significantly modify the hydrological cycle and monsoon climate in India and East Asia. Analysis of ice cores from the Tibet-Himalaya region also demonstrated the dust impact on climate and glacier melt [e.g., Qin *et al.*, 2000; Xu *et al.*, 2007].

[5] Because the TP plays a significant role in the Asian monsoon climate, it is important to better understand the transport pathway of TD dust over the TP. Dust is a major component of the aerosol burden over the plateau [e.g., Zhang *et al.*, 2001] and on the northern side of the surrounding area, where the Taklimakan and Gobi deserts are located

[e.g., Qian *et al.*, 2002]. Satellite has provided an important opportunity to look at the distribution of TD dust. Huang *et al.* [2007] first detected an event of the transport of TD dust over the TP in summer using data from Cloud-Aerosol Lidar and Infrared Pathfinder Satellite Observations (CALIPSO). The result showed that TD dust formed a dust layer at the height of 4–7 km amsl over the northern slope of TP. Later on, Liu *et al.* [2008] analyzed the seasonal distributions of dust over the TP and its vicinity to identify the patterns of dust transport up to and across the plateau using the first year of CALIPSO measurements (June 2006 through May 2007). Xia *et al.* [2008] also showed that the seasonal and inter-annual variations of aerosol optical depth (AOD) over the TP is more correlated with that over the TD in summer than in spring based on the retrievals from Multiangle Imaging SpectroRadiometer (MISR).

[6] However, satellite measurements can only provide some general information about the distribution of TD dust. In this study, a version of the Weather Research and Forecasting (WRF) model [Skamarock *et al.*, 2008] that simulates trace gases and particulates simultaneously with the meteorological fields (WRF-Chem) [Grell *et al.*, 2005] is used to investigate the detailed transport mechanism and estimate the radiative forcing of TD dust over the TP during a typical dust storm event on 26–30 July 2006. From 14 June to 30 September 2006, CALIPSO detected approximately 48 Tibetan dust plumes from a total of 90 nighttime overpasses over Tibet for the period. The frequency of occurrence of summer dust plumes over the TP (25°–45°N, 75°–100°E) is about 53%. This dust storm on 26–30 July 2006 developed over North Xinjiang and the Tarim Basin and extended southward afterward. Under the influence of this storm, a wind-blown sand and/or dust cloud persisted over northern Qinghai and Tibet through 1 August [Huang *et al.*, 2007]. The paper is organized as follows: Model and observational data are described in sections 2 and 3. Model evaluation and discussion of the emission, transport, accumulation, and radiative forcing of TD dust over the TP are presented in section 4. Conclusions and discussions are presented in section 5.

## 2. Model Description

[7] The WRF-Chem model (v3.2.1), a version of the WRF model [Skamarock *et al.*, 2008] that simulates trace gases and particulates simultaneously with the meteorological fields [Grell *et al.*, 2005], is used in this study. The Model for Simulating Aerosol Interactions and Chemistry (MOSAIC) aerosol model [Zaveri *et al.*, 2008] and Carbon Bond Mechanism (CBMZ) photochemical mechanism [Zaveri and Peters, 1999] were implemented by Fast *et al.* [2006] into WRF-Chem, which includes complex treatments of aerosol radiative properties and photolysis rates. MOSAIC uses a sectional approach where the aerosol size distribution is divided into discrete size bins. Eight size bins (0.039–0.078  $\mu\text{m}$ , 0.078–0.156  $\mu\text{m}$ , 0.156–0.312  $\mu\text{m}$ , 0.312–0.625  $\mu\text{m}$ , 0.625–1.25  $\mu\text{m}$ , 1.25–2.5  $\mu\text{m}$ , 2.5–5.0  $\mu\text{m}$ , and 5.0–10.0  $\mu\text{m}$  dry diameter) are employed in this study as in Fast *et al.* [2006, 2009]. Aerosol radiative feedback is simulated by the rapid radiative transfer model (RRTMG) [Mlawer *et al.*, 1997; Iacono *et al.*, 2000] for both short-wave (SW) and longwave (LW) radiation as implemented

by *Zhao et al.* [2011]. The aerosol optical properties such as extinction, single-scattering albedo, and the asymmetry factor for scattering are computed as a function of wavelength and three-dimensional position. Each chemical constituent of the aerosol is associated with a complex index of refraction. A detailed description of the computation of aerosol optical properties in WRF-Chem can be found in *Fast et al.* [2006] and *Barnard et al.* [2010].

[8] The GOCART (Georgia Tech/Goddard Global Ozone Chemistry Aerosol Radiation and Transport) dust emission scheme [*Ginoux et al.*, 2001] was coupled with MOSAIC within the WRF-Chem framework by *Zhao et al.* [2010]. As described in *Ginoux et al.* [2001], the GOCART scheme calculates the dust emission flux  $G$  as

$$G = CSs_p u_{10m} (u_{10m} - u_t)$$

where  $C$  is an empirical proportionality constant;  $S$  is a source function which defines the potential dust source regions and comprises surface factors, such as vegetation and snow cover;  $s_p$  is a fraction of each size class of dust in emission;  $u_{10m}$  is the horizontal wind speed at 10 m; and  $u_t$  is the threshold wind velocity below which dust emission does not occur and is a function of particle size, air density, and surface soil moisture. In this study, the size distribution of emitted dust (i.e., the total amount of emitted dust mass is distributed into the eight size bins mentioned above from smaller to larger sizes with mass fraction of 1.e–8, 1.e–6, 3.e–4, 3.5e–3, 0.018, 0.070, 0.26, and 0.64, respectively) and the dust optical properties (i.e., refractive index with a constant value of 1.53 + 0.003i for SW and various values for LW) follow *Zhao et al.* [2010, 2011] due to insufficient information about the optical properties of TD dust. More details about the coupling of the GOCART dust emission scheme with WRF-Chem can be found in *Zhao et al.* [2010]. Anthropogenic emissions of CO, NO<sub>x</sub>, SO<sub>2</sub>, volatile organic compounds (VOCs), black carbon (BC), organic carbon (OC), PM<sub>2.5</sub>, and PM<sub>10</sub> used in the simulations over the model domain are obtained from the Reanalysis of the Tropospheric (RETRO) chemical composition inventories (<http://retro.enes.org/index.shtml>). Biomass burning emissions are obtained from the Global Fire Emissions Database, Version 3 (GFEDv3) with monthly temporal resolution [*van der Werf et al.*, 2010]. In this study, although aerosols other than dust are simulated, the contribution of dust to the total aerosol mass and AOD is about 99% and 90%, respectively, over the TD region and about 97% and 80% over the TP region (Figure 1), which is consistent with that found by *Huang et al.* [2007] based on the depolarization ratio from the CALIPSO data. Therefore, dust is the dominant aerosol species over the TD and the north slope of the TP, and the contribution from other aerosol species to the aerosol total mass and radiative forcing is relatively small and is not discussed in the following.

[9] The WRF-Chem simulation was performed using one-way nesting (i.e., no feedback from the inner domain to the outer domain) with an outer domain (domain 1) at 27 km horizontal resolution, covering the TP and surrounding areas with 121 × 114 grid points (64.904°E–108.234°E, 22.424°N–50.496°N) and an inner domain (domain 2) at 9 km horizontal resolution with 241 × 148 grid points (69.539°E–96.834°E, 30.961°N–46.056°N) (as shown in

Figure 1). The simulation is configured with 50 stretched vertical layers up to 50 hPa. Two regions are defined to cover the TD with 91 × 46 grid points (TD region, 78.3°E–85.7°E, 35.9°N–39.6°N) and the TP with 91 × 46 grid points (TP region, 78.3°E–85.7°E, 31.5°N–35.0°N) for further analysis (Figure 1). Although the inner domain does not provide feedback to the outer domain, the inner-domain simulation with the high resolution is important to resolve the complex topography of the region, which includes sharp topographic gradients and small-scale terrain variations. The results from the inner-domain simulation are used for the analyses over the TD and TP regions, while the results from the outer domain are used for the analyses of large-scale features that are not fully covered by the inner domain. The initial meteorological fields and lateral boundary conditions are from the National Center for Environmental Prediction final analysis (NCEP/FNL) data at 1° horizontal resolution and 6 h temporal intervals. The chemical initial and boundary conditions are from the default profiles in WRF-Chem, which are the same as those used by *McKeen et al.* [2002] and are based on averages of midlatitude aircraft profiles from several field studies over the eastern Pacific Ocean. The simulation is conducted from 21–30 July 2006. Only the results from 26–30 July (referred to as the simulation period hereafter) are analyzed to avoid the impact from initial condition. The Mellor-Yamada-Janjic (MYJ) planetary boundary layer (PBL) scheme [*Janjic*, 1994], Noah land surface module [*Chen et al.*, 1996; *Chen and Dudhia*, 2001], Morrison two-moment microphysics scheme [*Morrison et al.*, 2005], Grell cumulus scheme [*Grell et al.*, 1994], and RRTMG longwave and shortwave radiation scheme [*Iacono et al.*, 2000] are used in this study. The modeled  $u$ -component and  $v$ -component wind and atmospheric temperature are nudged toward the NCEP/FNL analysis data with a nudging time scale of 6 h over both domains [*Stauffer and Seaman*, 1990].

### 3. Observations

#### 3.1. MODIS AOD

[10] The AOD data from the Moderate-resolution Imaging Spectroradiometer (MODIS) Level 3 “Deep-Blue” retrievals are used. The MODIS “Deep-Blue” algorithm retrieves global aerosol information over land including bright surfaces at 1° × 1° resolution [*Kaufman et al.*, 1997; *Hsu et al.*, 2006] and is found with positive biases compared with ground-based observations over northwestern China [*Ge et al.*, 2010]. MODIS on board the Aqua platform passes over the equator at 13: 30 local time (LT = UTC + 6 h over the TD). In comparison, the model results are sampled in the same overpass time as MODIS on Aqua.

#### 3.2. MISR AOD

[11] The AOD data from the MISR aerosol level 3 retrievals are also used. MISR on board the NASA Terra platform has been producing AOD globally since February 2000. A push-broom camera instrument is used to measure the same point on Earth at nine different along-track view angles, ranging from 70° aftward to 70° forward (with four forward, one nadir, and four aft cameras), and at four spectral bands (446, 558, 672, and 866 nm). The resolution of the Level 3 MISR AOD products is 0.5° × 0.5°. MISR on board the Terra

platform passes over the equator at 10:45 LT during the daytime. It can retrieve aerosol properties even over highly reflective surfaces like deserts [Martonchik *et al.*, 2004]. A detailed description of MISR aerosol retrieval is given by Martonchik *et al.* [1998, 2002]. In comparison, the model results are sampled in the same overpass time as MISR on Terra.

### 3.3. CALIPSO Aerosol Extinction Profile

[12] The aerosol extinction profiles retrieved by the Cloud-Aerosol Lidar and Infrared Pathfinder Satellite Observation (CALIPSO) satellite are used in this study. The CALIPSO satellite [Vaughan *et al.*, 2004, Winker *et al.*, 2003] was launched in April 2006, and data have been available from June 2006 onward. CALIPSO carries the Cloud-Aerosol Lidar with Orthogonal Polarization (CALIOP) instrument, which can measure the vertical structure of the atmosphere. In this study, aerosol extinction profiles from the CALIPSO level 2 product (version 3.01) are used to evaluate the model. The data can be downloaded from <http://eosweb.larc.nasa.gov/>. During the dust event investigated in this study (26–30 July), very few CALIPSO orbit paths crossed the TD and TP. We used the retrievals along the orbit path at 20:08 UTC (2:08 LT) on 27 July 2006. The retrievals along the orbit paths on other days during the dust storm (26–30 July) have even fewer data values. We screened our data for clouds and stratospheric features using the Atmospheric Volume Description. Cloud aerosol discrimination (CAD) score, which reflects our confidence that the feature under consideration is either an aerosol or a cloud, was also used. In this study, we screened out features with CAD score greater than  $-80$ . The CALIPSO extinction quality control (QC) flags were also used to find solutions where the lidar ratio is unchanged during the extinction retrieval (extinction QC=0) or if the retrieval is constrained (extinction QC=1). We note that the impact of the screening procedure in this specific case is negligible.

### 3.4. MERRA Reanalysis

[13] Modern-era Retrospective Analysis for Research and Applications (MERRA) is the most recent reanalysis data produced by NASA Global Modeling and Assimilation Office using the GEOS data assimilation system [Rienecker *et al.* 2011]. The model uses a finite-volume dynamical core that is run at a resolution of  $\frac{1}{2}^{\circ}$  latitude and  $\frac{2}{3}^{\circ}$  longitude with 72 vertical layers. Assimilation is done using grid-point statistical interpolation, a new three-dimensional variational analysis algorithm [Rienecker *et al.*, 2011].

## 4. Results

### 4.1. Model Evaluation

[14] In this particular case of a 5 day dust event over the TD, it is difficult to find in situ observations. Satellite observations from MODIS and MISR also have limited spatial and temporal coverage due to the difficulty to retrieve aerosol properties over bright surfaces and beneath thin clouds during the simulation period. We start with comparing the daily spatial distribution of 550 nm AOD from the MODIS retrievals with the corresponding WRF-Chem simulation on 26–30 July in Figure 2 (MISR has too few data and is not shown). Although part of day-to-day variation is captured by the MODIS retrieval and simulation (e.g., the

elevated AOD across the TD on 28 June), day-to-day variation from the MODIS retrievals is not obvious enough to be used to evaluate the model results. Therefore, instead of evaluating the detailed transport processes (such as day-to-day variation, which will be discussed in section 4.3.1), we conducted a simulation with only the outer domain at 27 km resolution for the entire month of July. The 9 km nested domain is not included because of computational cost. However, the aerosol mass and AOD in the 9 km domain is similar to that of the 27 km domain during the dust event (not shown). The one month simulation is then compared with satellite retrievals to evaluate the model skill to reproduce the dust AOD over the source region. Figure 3 presents the spatial distributions of monthly mean AOD at 550 nm from the MISR and MODIS retrievals and the corresponding WRF-Chem simulations during July 2006. The simulation results are sampled at 13:30 LT (UTC+6 h over the TD) and 10:45 LT when compared with MODIS and MISR retrievals, respectively. In general, MISR and MODIS show consistent spatial patterns of AOD over the TD and its surrounding areas, but the magnitude of MODIS retrieved AOD ( $\sim 0.76$ ) is higher than that of MISR ( $\sim 0.56$ ) over the TD region (Figure 1), especially over the east boundary area of TD. Part of the difference between the MODIS and MISR retrievals may be due to their different overpass time. Ge *et al.* [2010] found that the MISR retrieved AOD has more reasonable agreements with ground-based observations over northwestern China compared with the MODIS “Deep-Blue” products. In this simulation, the average of simulated AOD over the TD region is  $\sim 0.62$ , which is comparable to that from the MISR retrievals. The model reproduces the spatial pattern of satellite retrieved AOD over the TD, indicating that the dust source region is generally well represented by the dust source function in the GOCART scheme over the TD. Anthropogenic emissions are the dominant aerosol source over northern India. The simulated AOD is much lower than the retrieved AOD from satellites in the southwest part of the domain, reflecting the likely underestimation of anthropogenic emissions of northern India.

[15] Figure 4 presents the vertical distributions of aerosol extinction coefficient simulated and observed along the orbit path of CALIPSO/CALIOP (as shown in Figure 1) over the TD and TP at 20:08 UTC on 27 July 2006. Although there are limited aerosol extinction coefficient data retrieved along this orbit path from the CALIPSO L2 product, the comparison shows that the model reasonably reproduces the aerosol extinction profiles over major regions of the TD ( $\sim 38^{\circ}\text{N}$ ) and northern TP ( $32^{\circ}\text{N}$ – $35^{\circ}\text{N}$ ). Both retrievals and simulation show high dust loading at the lower atmosphere above the TD, and the dust reaches the free troposphere up to 9 km at  $35^{\circ}\text{N}$ – $40^{\circ}\text{N}$ . In addition, the simulated aerosol vertical distribution is consistent with that of total attenuated backscattering from the CALIPSO L1 data (there are no retrievals of aerosol extinction profiles from the L1 data) and the feature mask from the CALIPSO Level 2 data (figures are not shown). Through comparing to the CALIPSO L1 total attenuated backscattering data and the CALIPSO L2 feature mask data, we suspect that some high aerosol extinction coefficients from the CALIPSO L2 retrievals (e.g., over north of  $40^{\circ}\text{N}$ ) that are not found in the simulation may be uncertain. In addition, the CALIPSO L2 retrievals may have

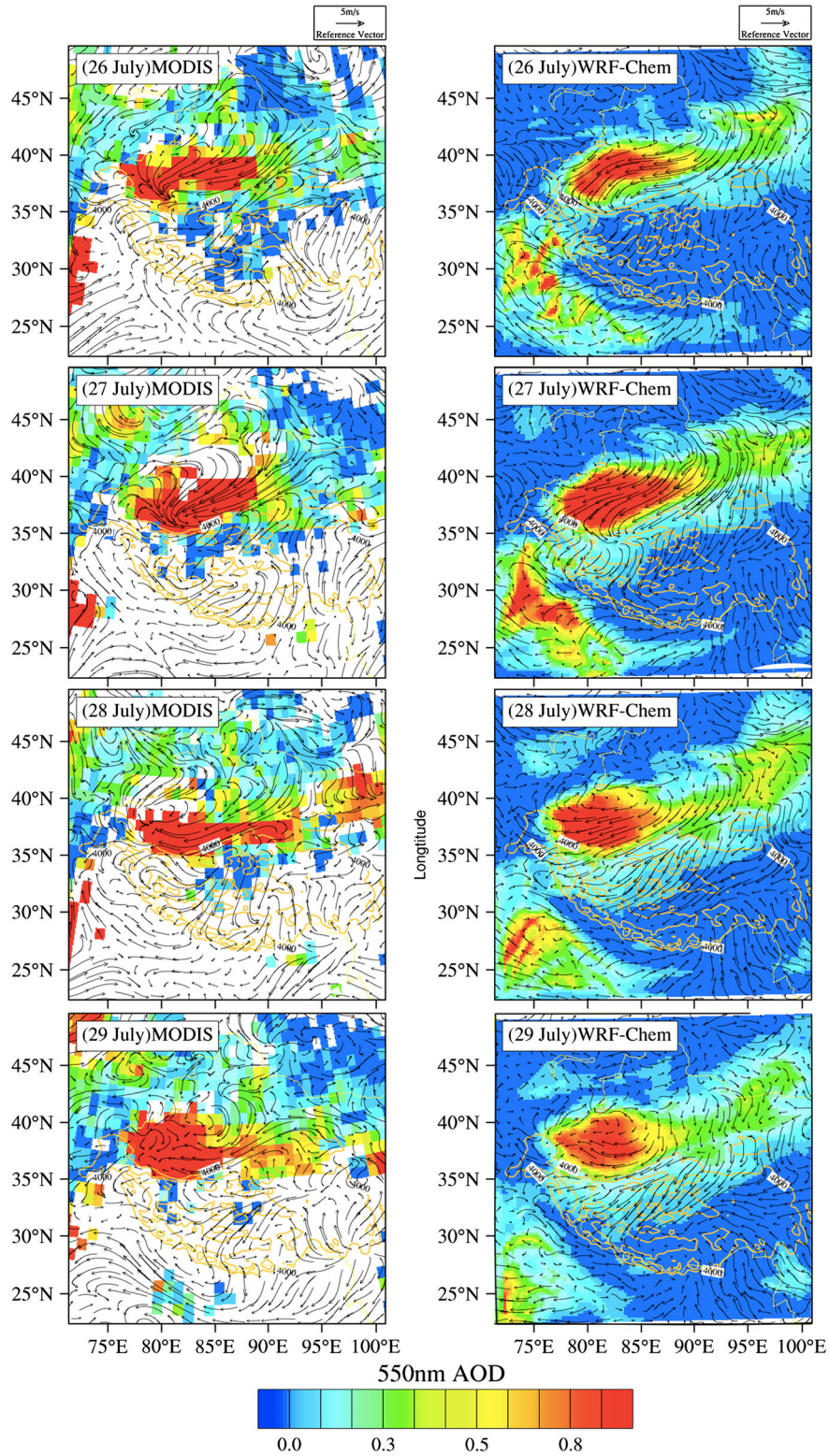


**Figure 2.** Spatial distribution of aerosol optical depth (AOD) at 550 nm from the satellite retrievals of MODIS on Aqua (left) and Weather Research and Forecasting model with chemistry (WRF-Chem) simulation (right) over domain 1 from 26–29 July. The surface wind at left column is from the Modern-era Retrospective Analysis for Research and Applications (MERRA) reanalysis data and at right is from the WRF-Chem simulation. The raster shaded areas depict the regions with topography higher than 5 km.

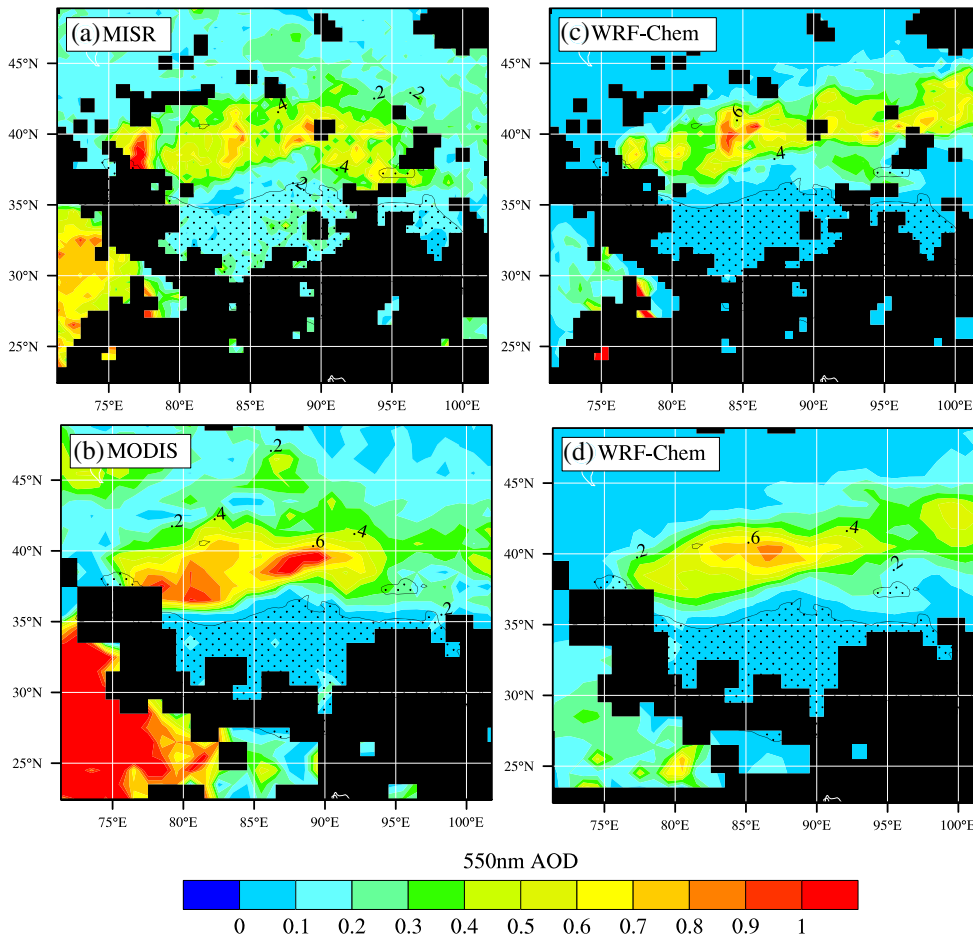


**Figure 3.** Spatial distribution of monthly mean 550 nm AOD from the satellite retrievals of (a) Multiangle Imaging SpectroRadiometer (MISR) on Terra and (b) MODIS on Aqua and (c and d) the corresponding WRF-Chem simulations over domain 1 for July 2006; raster shaded areas represent the region with topography higher than 5 km. The MODIS retrievals are from the “Deep-Blue” products. The model results are sampled at the overpass time of the MISR and MODIS retrievals.

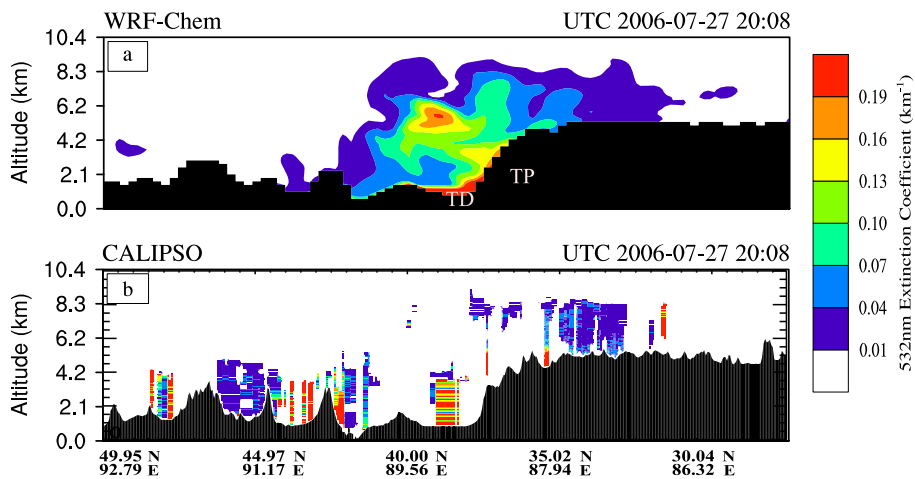


**Figure 4.** Cross-section of aerosol extinction coefficients ( $\text{km}^{-1}$ ) over the TP and its surrounding areas at 20:08 UTC on 27 July 2006 from (a) the CALIPSO retrievals along its orbit path (as shown in Figure 1) and (b) the corresponding WRF-Chem simulations over domain 1.

eliminated some useful information from the L1 retrievals on the northern TP slope because of the overly strict criteria.

[16] Wind is the most crucial meteorological factor for dust emission and transport. Figure 5 shows the averaged spatial distribution of wind circulation at 500 hPa from the MERRA reanalysis data and WRF-Chem simulations for 26–30 July 2006. In general, the model well captures the wind circulation shown in the MERRA reanalysis data. Westerly winds dominate to the north of the TD. A significant anticyclone exists in the south of the TD, resulting in a northerly wind that benefits the transport of TD dust into the TP region. Overall, the model can reasonably reproduce the observed 3-D structure of the dust veil, although it is difficult to have a side-by-side comparison of the daily evolution of the dust storm due to the limits of the observational data during this dust event. The simulated results are used to further investigate the detailed processes related to the dust ejection and transport in the following sections.

#### 4.2. Dust Emission over the TD

[17] The emission of dust is highly dependent on meteorological conditions over the source region. In this section, we analyze the meteorological conditions that determine the dust emission and transport over the TD to provide a balanced synthesis. In order to show the large-scale synoptic condition (not fully covered by the WRF-Chem simulation domain), the NCEP/FNL reanalysis data are used to present the spatial distribution of geopotential height and temperature at 500 hPa at 12:00 UTC on 26–29 July in Figure 6. The spatial distribution of daily dust emission and 12:00 UTC 10 m winds on July 26–29 from the WRF-Chem simulation is also shown in Figure 7 to examine the daily evolution of dust emissions over the TD and its response to the change of upper-level synoptic pattern.

[18] On 26 July, a deep low-pressure system at 500 hPa is formed in West Siberia (60°E–70°E, 60°N–70°N) and extended southward to the north of China. The shortwave trough was located near the Balkhash Lake (46°10′N,

74°20′E). A broad area around South Xinjiang was dominated by southwesterly winds in front of the trough. At the surface, the existence of Mountain Tian Shan induced strong northeasterly winds along the corridor surrounding the southeastern side of the mountain, which brought a large amount of cold air into the Tarim Basin (Figure 6a). The maximum simulated dust emission flux reached around  $83 \mu\text{g m}^{-2} \text{s}^{-1}$  over the TD (Figure 7a). On 27 July, the deep low-pressure system developed with a cold trough located over Siberia. A strong temperature gradient existed along the trough axis with cold advection in front of the trough. Cold air was transported by the westerly winds along south Xinjiang (Figure 6b). The cold air accumulated at the foot of Mountain Tian Shan was lifted to a significant height and crossed over the mountain into the Tarim Basin. Cold air in the basin colliding with the warm air over the TD led to the formation of a cold front (Figure 7b). Figure 8 shows a MODIS/Aqua RGB color composite cloud image at 08:10 UTC on 27 July. The cold front can also be detected over the TD at 08:10 UTC on 27 July. The cloud distribution shows that the cold front existed over the TD around 75°E–85°E and 40°N–45°N. The cold front crossed the TD and resulted in strong northeasterly winds and dust mobilization with the maximum dust emission flux reaching  $116 \mu\text{g m}^{-2} \text{s}^{-1}$  during the day. On 28 July, the superposition of the temperature and geopotential height gradients led to a weakening of the shortwave trough (Figure 6c). The cold front moved to the northern slope of Mountain Kunlun and gradually decayed, resulting in a weakening of the dust emission over the TD. The model results show an evident anti-cyclone at the low level over the TD. Strong air motion toward the TP can also be found (Figure 7c). On 29 July, the 500 hPa trough became weaker (Figure 6d), and a weak high-pressure ridge appeared on 30 July over the northern TD (figure is not shown), indicating the end of the frontal system and the dust veil. However, strong winds remain toward the TP, probably due to the thermal effect of the TP, which could potentially bring the dust aerosol to the northern slope of TP

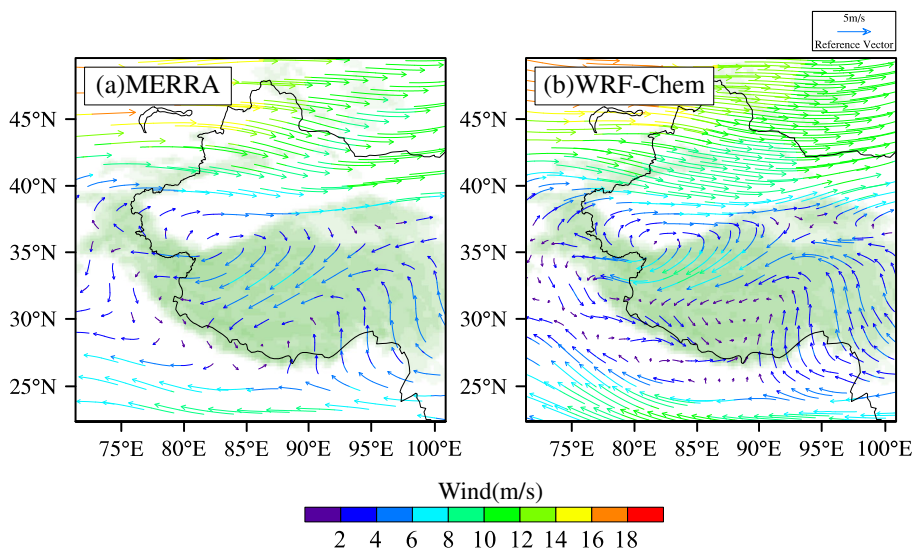


**Figure 5.** Spatial distribution of daily averaged wind circulation at 500 hPa from (a) MERRA reanalysis data and (b) WRF-Chem simulations over domain 1 averaged over the period of 26–30 July 2006. Shaded areas (light green) represent the regions with topography higher than 2 km.

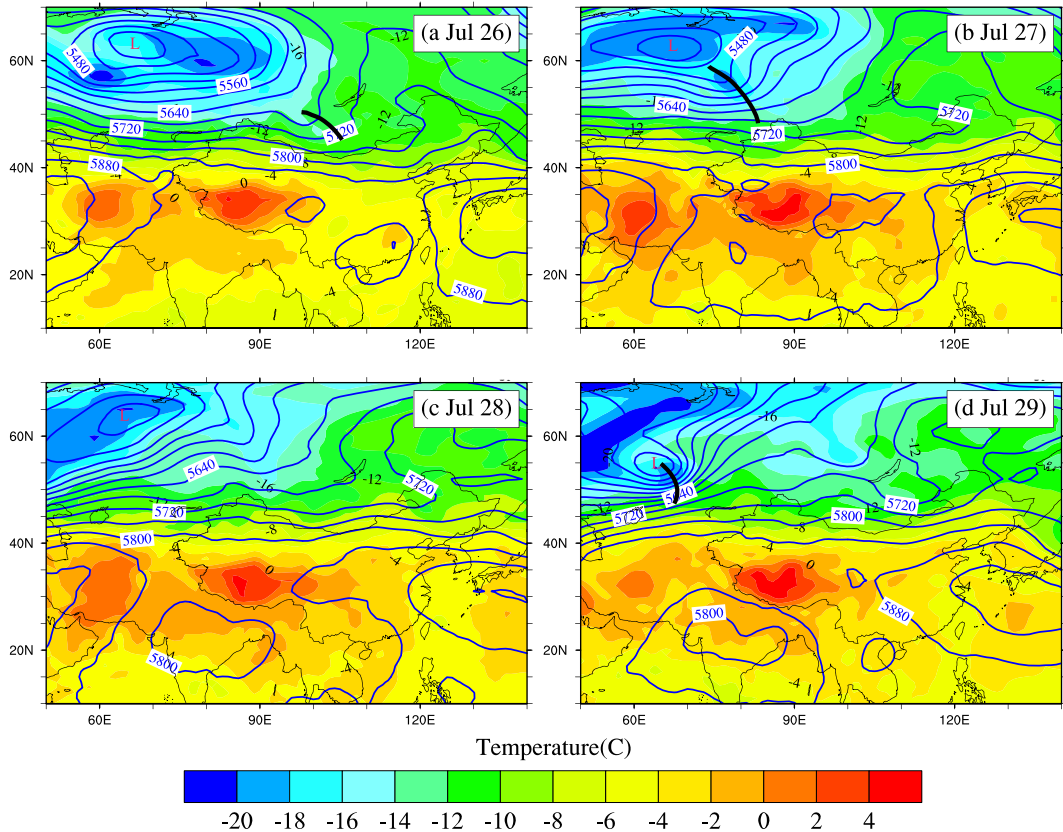


**Figure 6.** Spatial distribution of geopotential height (blue contour) and temperature (color) at the level of 500 hPa from NCEP/FNL reanalysis data over China and its adjacent areas at 12:00 UTC of 26–29 July 2006. The locations of low-pressure regions (letter L) and associated troughs (solid black lines) are marked.

(Figure 7d, see discussion in section 4.3). Overall, the dust storm event was generated by a mesoscale cold wind system, which propagates around the eastern side of the Tian Shan Mountains and directly crossing over them. This condition leads to a very strong cold front system with the large dust storms over the TD. These meteorological conditions favor the transfer of TD dust over the TP.

#### 4.3. Transport and Accumulation of TD Dust over the TP

##### 4.3.1. Impact of the Weakening of Predominant East Asian Westerly Jet

[19] To show the daily evolutions of dust transport in this dust storm event, Figure 9 presents daily mean values of vertical-latitude cross-section of the modeled aerosol extinction coefficient and potential temperature at 85.5°E. The red line represents the daily averaged planetary boundary layer height (PBLH) that is estimated by the MYJ PBL scheme based on the turbulent kinetic energy (TKE) profile. The top of the PBL is the height where the TKE decreases to a prescribed low value [Janjic, 2001]. The cross-section at 85.5°E is selected to cut across the center of the TD and TP to represent the transport of the TD dust over the TP.

[20] On 26 July, the dust storm started over the eastern basin, and dust particles were transported into the southwest part of the TD by the strong northeasterly winds (Figure 2). High aerosol extinction coefficient ( $>0.2 \text{ km}^{-1}$ ) extends to  $\sim 6 \text{ km}$  over most of the TD regions. A deep mixed layer of

uniform potential temperature existed over the TP. TD dust began to be transported by the strong surface wind along the northern slope of the TP from near surface to the upper boundary layer, which is dominated by turbulent mixing (Figure 9a). The dust layer above the TP was first dominated by westerly winds, and then easterly winds dominated. The dust originating from the TD propagated toward the plateau under the impact of easterly winds. Dust mobilization became more active over the entire TD regions on 27 July because of the stronger northeasterly winds generated following the southward movement of the cold front (Figure 7b). A large amount of dust accumulated at the foot of the Mountain Kunlun, where the AOD shows relatively higher value of  $\sim 0.9$  (Figure 2). Dust particles were continuously transported toward the TP and lifted up to the TP due to orographic lifting. Afterward, dust broke through the PBL and was injected into the upper troposphere, reaching an altitude of 8 km (Figure 9b). The flow trajectories were close to the ground on 26–27 July (figure is not shown). On 28–29 July, although the surface dust mobilization became weaker (Figures 7c and 7d), dust in the air was continuously transported by the strong northeasterly winds to the TP (Figure 2) and broke through the PBL to the upper troposphere (up to about 10 km amsl) (Figures 9c and 9d). The flow trajectories were no longer close to ground afterward, leading to weakening of the dust generation process (figure is not shown). Overall, the first 2 days were dominated by the dust

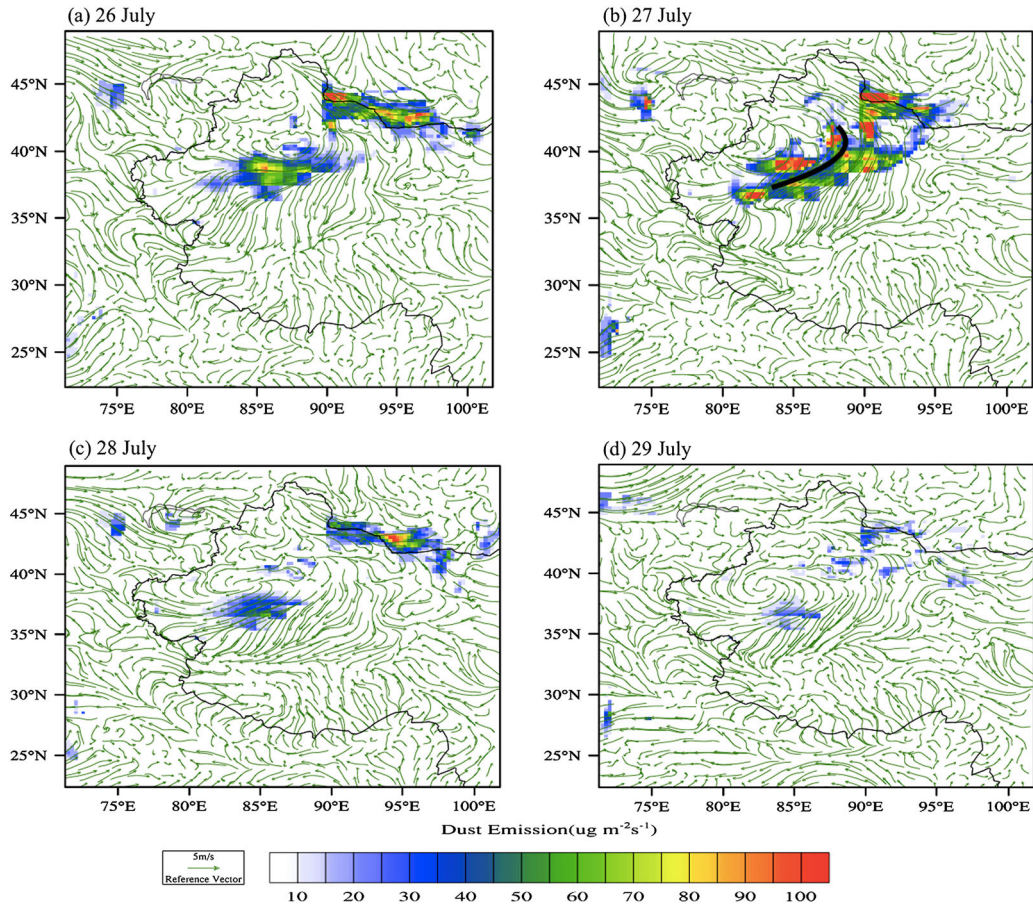


**Figure 7.** Spatial distribution of dust emission (color) and 10 m wind (green vectors) at 12:00 UTC on 26–29 July 2006 from the WRF-Chem simulations over domain 1. The black line represents the cold front.

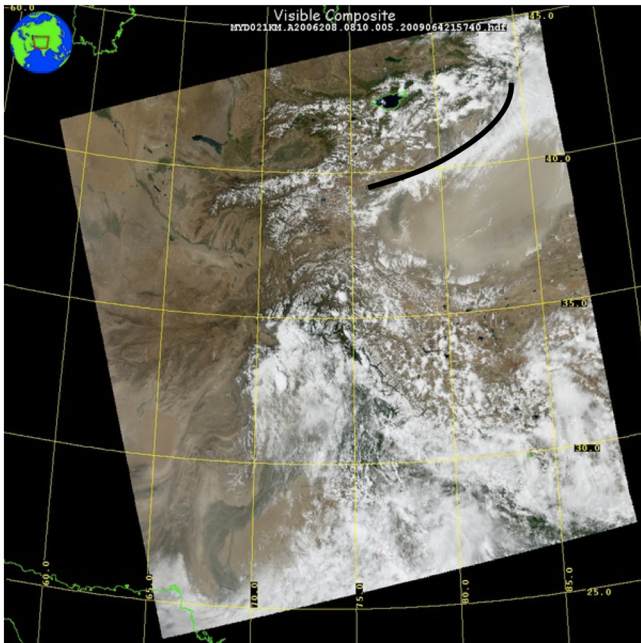


**Figure 8.** Spatial distribution of clouds and dust storms derived from the remote sensing based MODIS/Aqua red-green-blue color composite image at 08:10 UTC on 27 July (25°–35°N, 65°–85°E). The black line represents the cold front.

generation, while the next 2 days were dominated by the dust transport. It is noteworthy that, although the dust concentration over the TP is much smaller than that over the TD, it still has potentially significant impact on regional and global climate [e.g., *Lau et al.*, 2006, 2010; *Qian et al.*, 2011].

[21] Figure 10 shows the vertical-latitude cross-section at 85.5°E of meridional circulation, zonal wind, and potential temperature from the WRF-Chem simulation averaged over the period of 26–29 July. The maximum of westerly wind center at 42°N is about 46 m/s, indicating the weak westerly wind transport that favors the meridional transport of TD dust. Easterly winds (blue shade in this figure) are also apparent near the surface over the southern TD and the northern slope of the TP. It indicates that these weather conditions play an important role in the southward transport of summer TD dust. *Zhang et al.* [2008] showed the shifts of the East Asian westerly jet patterns from winter to summer. They also found the core of zonal winds at 200 hPa along 90° jumps from around 30°N in winter to nearby 40°N in summer. The East Asian westerly jet over the TD often shifts northward and becomes weaker (about 30–40 m/s in July) in summer compared to its position near 32°N with maximum wind speed about 50–70 m/s in spring. The NCEP/FNL reanalysis data in 2006 show similar seasonal patterns of zonal winds (not shown).

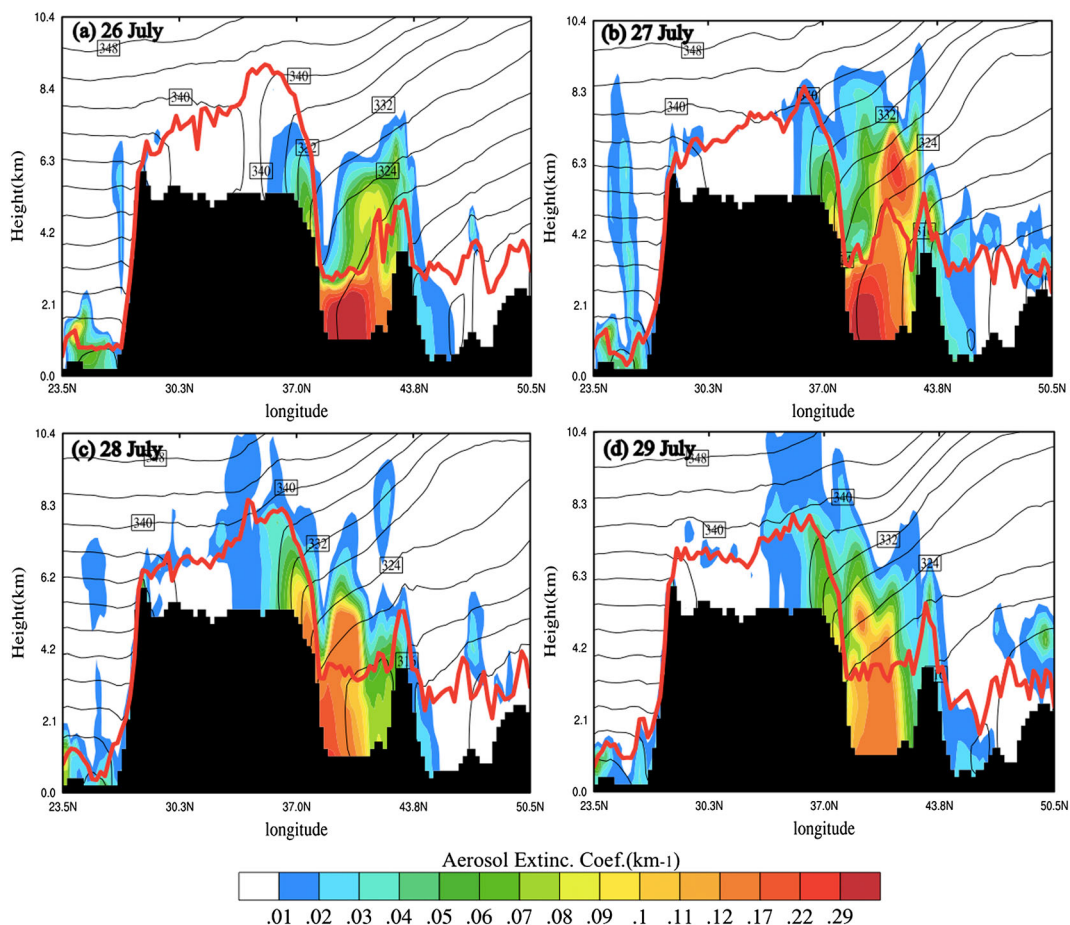


**Figure 9.** (a–d) Vertical-latitude cross-section at  $85.5^{\circ}\text{E}$  of daily averaged aerosol extinction coefficient and potential temperature on 26–29 July from the WRF-Chem simulations over domain 1. Black contours indicate the potential temperature. The red line represents the daily averaged planetary boundary layer height (PBLH).

#### 4.3.2. Impact of the TP Thermal Condition

[22] The thermal condition of TP (behaves as a “heat pump”) could also benefit the southward transport of TD dust in summer. The simulated mean relative vortices and wind circulation at 500 hPa during the simulation period are shown in Figure 11. There is an evident belt of positive vorticity over the TP (Figure 11a), which has been recognized as the Tibetan Plateau low vortex (PLV), a typical summer weather system due to the thermal condition of TP forming, developing, and decaying over the western, middle, and eastern Plateau, respectively, along the wind shear [Tao and Ding, 1981]. The negative vorticity over the Mountain Kunlun was caused by topography shearing. There is vertical motion due to the positive vorticity over the TP, and an isothermal layer existed over the TP caused by the strong thermal mixing, so a large amount of dust particles accumulated over the TP and even broke through the PBL to the upper troposphere (Figure 11b). This accumulation of TD dust over the TP was also found by Huang *et al.* [2007] using CALIPSO observations. Li and Yu [2001] also found that the TP plays important roles in transporting pollutants from surface to upper troposphere and stratosphere in summer due to the thermal influences of TP as a heat source.

[23] The “heat pump” effect of the TP on dust upward transport can also be demonstrated by the variation of dust

concentration in the upper troposphere. Figure 12 shows daily dust concentration at 8–10 km amsl and the ratio of dust concentration at higher levels (5–7 km above surface) to that at lower levels (1–3 km above surface) over the TP region ( $76.6^{\circ}\text{E}$ – $85.7^{\circ}\text{E}$ ,  $32.3^{\circ}\text{N}$ – $36.3^{\circ}\text{N}$ , Figure 1) and the TD region ( $76.0^{\circ}\text{E}$ – $85.6^{\circ}\text{E}$ ,  $36.07^{\circ}\text{N}$ – $40.7^{\circ}\text{N}$ , Figure 1) from the inner-domain simulation with 9 km horizontal resolution, respectively. The upper tropospheric dust concentration has much less variation ( $1$ – $6 \mu\text{g}/\text{m}^3$ ) over the TD than that over the TP ( $5$ – $21 \mu\text{g}/\text{m}^3$ ) during the simulation period. The peak of dust concentration (on 28 July) over the TP is much larger (about  $21.3 \mu\text{g}/\text{m}^3$ ) than that over the TD (about  $5.2 \mu\text{g}/\text{m}^3$ ), reflecting the thermal influence of the TP. To compare the concentrations of dust lifted at the same height above the ground (instead of the amsl as shown in Figure 12a), Figure 12b shows the ratio of dust concentration at higher levels (5–7 km above surface) to that at lower levels (1–3 km above surface). It also shows that dust particles were lifted to a higher level over the TP after 28 July. The peak of ratio is visible on 29 July over the TP (about 0.21), which indicates a very strong vertical motion developed. Therefore, dust can be transported into the upper atmosphere over the TP due to the combined effect of local unstable stratification and large-scale convergence.

[24] Figure 13a shows the vertical-latitude cross-section at  $85.5^{\circ}\text{E}$  of mean aerosol extinction coefficient over the TD

and TP regions from the inner-domain simulation with 9 km horizontal resolution during the simulation period. TD dust was transported southward by a distance of 5–10 km and reached the middle of the TP (~32°N). Dry deposition plays an important role in determining the atmospheric dust

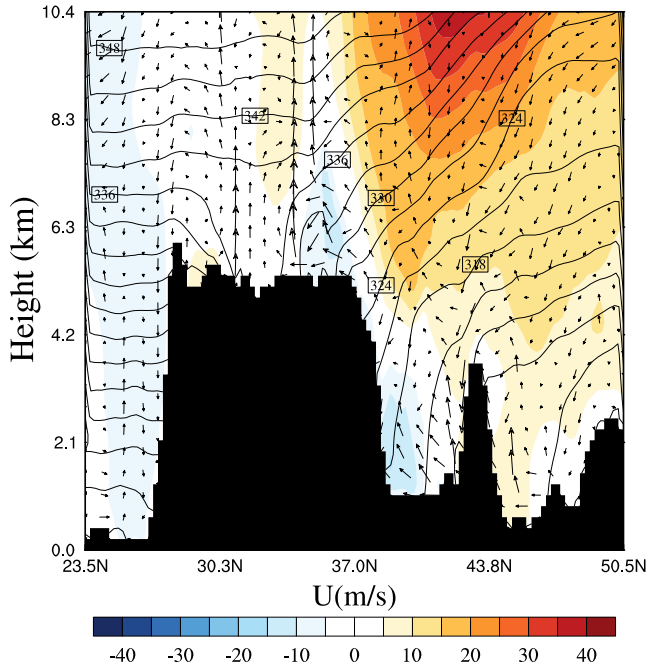


**Figure 10.** Vertical-latitude cross-section at 85.5°E of meridional circulation, zonal wind, and potential temperature averaged for 26–29 July 2006 from the WRF-Chem simulation over domain 1. Black contours depict potential temperature from 300 K to 350 K. Positive values represent westerly winds.

loading during the transport and also the amount of dust deposited on the snow. In this simulation, TD dust flux arrived at the TP (at 36.5°N) with a value of 6.6 Gg/day during 26–30 July, which is ~6% of the total TD dust emission (114 Gg/day) during the event, but decayed quickly to 3.4 Gg/day (by half from 36.5°N to 35.2°N) due to dry deposition, which may change the surface albedo especially when the land surface is covered by snow or glacier. About one eighth of the dust flux reached 32.7°N (0.84 Gg/day). This implies that southward transport of TD dust can cover a large area of the TP. Figure 13b compares daily variations of the dust outflow flux at the cross-section between 69.5°E–96.8°E at 32.7°N (red line), 33.9°N (pink line), 35.2°N (blue line), and 36.5°N (yellow line). Dust outflow flux has obvious diurnal cycle. The southward (from the TD to the TP) dust flow peaked at approximately 16:00 LT (UTC + 6 h) during the event due to diurnal variations of the upslope flow driven by the daytime heating of TP. Both field observations and numerical simulations [Yang *et al.*, 2004; Yanai and Li, 1994] showed that the convection activity over the plateau evolves from dry shallow convection in the morning to wet deep convection in the afternoon, which rapidly enhances in the afternoon and reaches maximum at about 18:00 LT. Our simulation also shows that the maximum height of PBL occurred at 16:00 LT (figure is not shown). The magnitudes of turbulent mixing over the TP attain the minima in the morning and the maxima in the late afternoon. Turbulent mixing dominates the dust flux transport from the near-surface layer to the upper boundary layer. On the other hand, the stronger thermal effect of TP in the afternoon leads to stronger convergence, which transports dust from the TD to the TP. In contrast, the cooling of the TP surface at night and early morning results in down-slope flow and a minimum southward dust flow or even a northward (negative, i.e., from the TP to the TD) dust flow at around 06:00 LT.

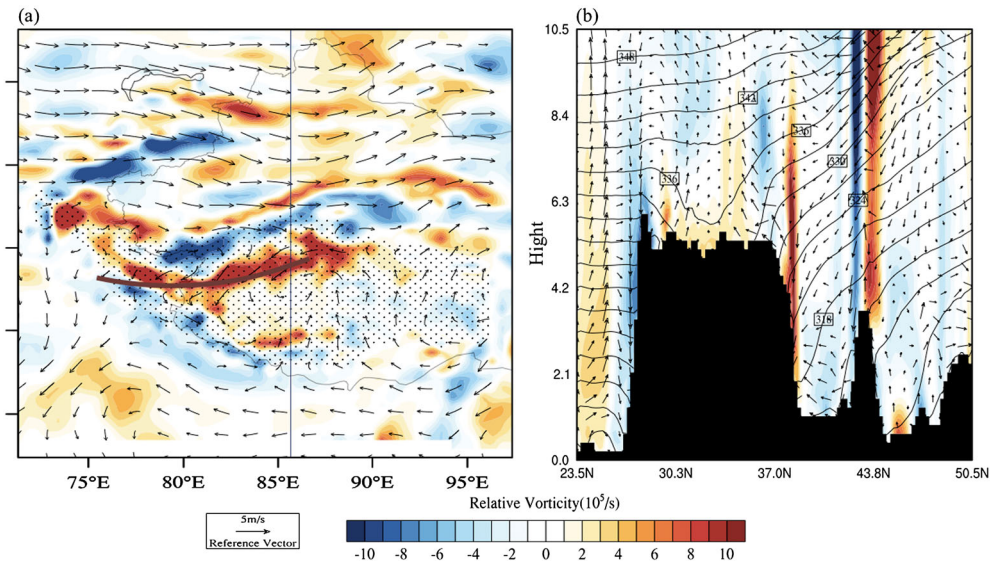


**Figure 11.** (a) Spatial distribution of the relative vortices and wind circulation at 500 hPa and (b) vertical-latitude cross-section at 85.5°E of relative vorticity, meridional circulation, and potential temperature averaged for 26–29 July 2006 from the WRF-Chem simulation over domain 1. In Figure 11a, the raster shaded areas depict the regions with topography higher than 5 km. The red line represents wind shear. In Figure 11b, black contours represent potential temperature from 300 K to 350 K.

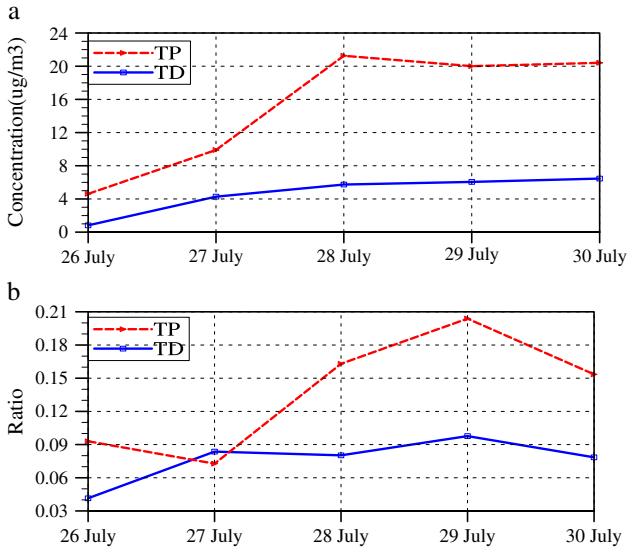


**Figure 12.** (a) Daily averaged dust concentrations at 8–10 km amsl and (b) daily ratio of dust concentrations at 5–7 km to that at 1–3 km above surface on 26–30 July 2006 over the TD region (blue solid line) and TP region (red dash line) from the WRF-Chem simulations over domain 2.

#### 4.4. Radiative Forcing of Dust over the TP

[25] The accumulation of TD dust over the TP could absorb and scatter solar radiation and modify the atmospheric heating profile. The dust-induced changes of radiative fluxes at the top of the atmosphere (TOA), surface, and in the atmosphere over the TP region averaged for the simulation period (26–30 July) from the inner-domain simulations with 9 km horizontal resolution are summarized in Table 1. The dust-induced forcing is calculated by subtracting the results from the WRF-Chem simulation without dust emission from the standard WRF-Chem simulation. In the atmosphere, dust induces SW warming and LW cooling with  $6.69 \text{ W m}^{-2}$  and  $-5.08 \text{ W m}^{-2}$ , respectively, with a net radiative warming effect of  $1.61 \text{ W m}^{-2}$ . At the surface, dust has a SW cooling effect with a domain average value of  $-11.71 \text{ W m}^{-2}$  (due to the absorption and scattering of dust), while it has a LW warming effect with a domain average value of  $6.13 \text{ W m}^{-2}$  due to trapping of LW radiation emitted from the surface. The dust-induced change of net (LW+SW) radiation fluxes at the surface is  $-5.58 \text{ W m}^{-2}$ . At the TOA, the net (LW+SW) dust radiative forcing is  $-3.97 \text{ W m}^{-2}$ , indicating that dust scattering has larger impact on the Earth-atmosphere system compared to dust absorption of SW. Overall, dust significantly warms the atmosphere and cools the surface and results in a negative TOA forcing over the TP.

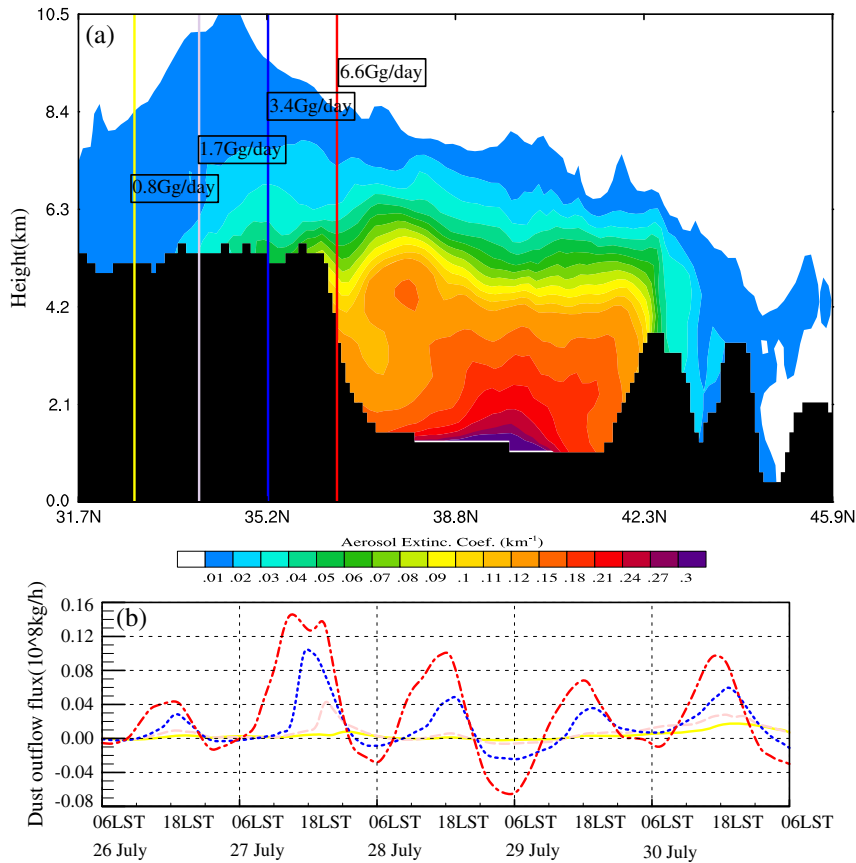


**Figure 13.** (a) Vertical-latitude cross-section at  $85.5^\circ\text{E}$  of the aerosol extinction coefficient on 26–30 July 2006 from the WRF-Chem simulation over domain 2. The values of horizontal dust fluxes are also shown at  $36.5^\circ\text{N}$ ,  $35.2^\circ\text{N}$ ,  $33.9^\circ\text{N}$ , and  $32.7^\circ\text{N}$ . (b) Daily averaged dust outflow flux from the TD to TP for 26–30 July 2006 from the WRF-Chem simulation over domain 2. Color lines are corresponding to the colored cross-sections at  $36.5^\circ\text{N}$ ,  $35.2^\circ\text{N}$ ,  $33.9^\circ\text{N}$ , and  $32.7^\circ\text{N}$  indicated in Figure 13a.

**Table 1.** WRF-Chem Simulated All-sky Radiative Forcing of TD Dust over the TP Region (Figure 1) on 24 h Average<sup>a</sup>

	SW ( $\text{W m}^{-2}$ )	LW ( $\text{W m}^{-2}$ )	TOTAL ( $\text{W m}^{-2}$ )
TOA	-5.02	1.05	-3.97
Atmosphere	6.69	-5.08	1.61
Surface	-11.71	6.13	-5.58

<sup>a</sup>“TOA” represents “top of atmosphere.” Positive means downward direction for TOA and surface, and absorption/heating for atmosphere. The results are from the inner-domain simulation with 9 km horizontal resolution.

[26] This dust-radiation interaction modifies the atmospheric heating profiles. Figure 14 shows the dust-induced change of atmospheric radiative heating profiles over the TP region (Figure 1) on 24 h average of 26–30 July derived from the WRF-Chem simulations with and without dust on

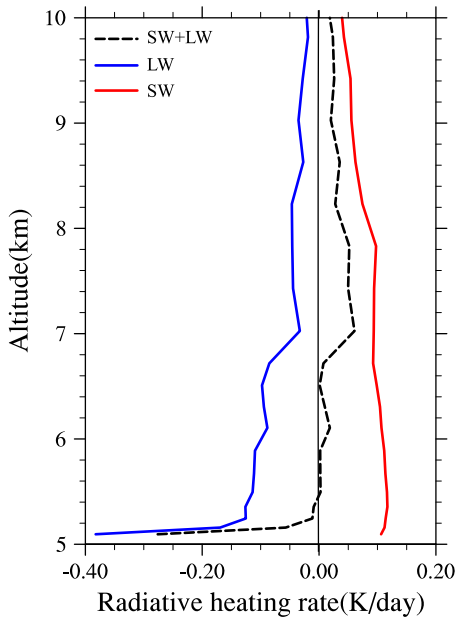


**Figure 14.** Vertical profiles of dust-induced changes of SW (red solid line), LW (purple solid line), and net (SW + LW, black dashed line) atmospheric radiative heating profiles on 24 h average of 26–30 July 2006 over the TP region derived from the WRF-Chem simulations with and without dust over domain 2.

the inner domain with 9 km horizontal resolution. Generally, dust induces a SW radiative heating of atmosphere with a maximum rate around  $0.1 \text{ K day}^{-1}$  near the surface and a LW radiative cooling of atmosphere with a rate of up to  $-0.4 \text{ K day}^{-1}$  near the surface. The dust-induced rates of SW heating and LW cooling in the atmosphere reduce gradually with altitude. On net effect, dust significantly cools the atmosphere near the surface and heats the atmosphere above with a maximum heating rate of  $0.11 \text{ K day}^{-1}$  at about 7 km. The comparison of our estimated dust radiative forcing and heating rate over the TP with previous studies is summarized in Table 2. In general, our results are comparable to those estimated near the TD dust source region in the previous literatures [Lau *et al.*, 2006; Ge *et al.*, 2011]. However, it should be noted that the different region, time period, and methods used to calculate radiative forcing may contribute to differences of the results.

## 5. Conclusions

[27] In this study, the WRF-Chem model with a relatively fine horizontal resolution is used to simulate an intense dust storm event during 26–30 July 2006 over the TD, under the meteorological condition that favors the injection and accumulation of dust. The simulated results are analyzed to investigate the mechanism of the transport of TD dust over the TP and its radiative forcing over the TP. The model well captures the features of large-scale synoptic conditions compared with the reanalysis data. The simulation is also evaluated with multiple satellite AOD retrievals (MODIS, MISR, and CALIPSO) for the emission and transport of TD dust for the first time. Since the satellite retrievals have limited spatial and temporal coverage due to the difficulty to retrieve aerosol properties over bright surfaces and beneath thin clouds during this 5 day dust storm event, it is difficult to evaluate the daily variation of TD dust transport. However, the model reasonably simulates the horizontal and vertical distributions of the TD dust over major regions of the TD and the northern TP on average.

[28] During 26–30 July 2006, both observation and simulation show an intense dust storm over the TD. Overall, this dust event was generated by a mesoscale cold front system that crossed over the Mountain Tian Shan and intruded into the TD. Dust was transported southward and arrived at the upper troposphere up to  $\sim 10 \text{ km}$  amsl over the TP. The

**Table 2.** Summary of Dust Radiative Heating Rates and Radiative Forcing in This and Previous Studies

Heating Rate (K/day)	TOA ( $\text{W/m}^2$ )	ATM ( $\text{W/m}^2$ )	Surface ( $\text{W/m}^2$ )	Region	Time	Method	References
SW + LW 0.11	-3.97	1.61	-5.58	TP	26–30 July 2006	WRF-Chem	This study
SW 0.2~0.4	-1.6	1.1	-12.6	Northern TP	April–May	<sup>b</sup> fVGC	Lau <i>et al.</i> [2006]
SW + LW 0.1~0.15	–	–	-60~ -90	TD	March–May of 2007–2009	<sup>b</sup> RTM, CALIPSO, MISR	Kuhlmann and Quaas [2010]
–	2.1	22.3	-20.2	<sup>c</sup> Zhangye	24 April 2008	<sup>a</sup> MFRSR	Ge <i>et al.</i> [2011]
–	-3.5	9.6	-13.1			<sup>a</sup> CIMEL	
–	3.3	21.0	-17.7	<sup>d</sup> Minqin	22 May 2008	MFRSR	
–	-1.8	7.3	-9.1			CIMEL	

<sup>a</sup>MFRSR represents the retrievals from Multi Filter Rotating Shadowband Radiometer, and CIMEL represents the retrievals from the AERONET instrument that is recognized as a highly accurate Sun photometer. The sign of the TOA radiative forcing derived by the MFRSR and CIMEL is opposite due to the different imaginary refractive indices and single scattering albedos (SSAs) of the derived aerosol optical properties (more details can be found in Ge *et al.* [2011]).

<sup>b</sup>fVGC represents finite-volume General Circulation Model; RTM represents Radiative Transfer Model.

<sup>c</sup>Zhangye ( $39.08^\circ \text{N}$ ,  $100.27^\circ \text{E}$ ) is located in a semi-desert area of northwest China.

<sup>d</sup>Minqin ( $36.61^\circ \text{N}$ ,  $102.96^\circ \text{E}$ ) is about 300 km away to the southeast of Zhangye.

passage of the cold front combined with the relatively weak westerly winds over the TD, an important addition to the background “heat pump” due to the thermal effect of the TP, favors the uplifting and transport of the TD dust over the TP. During the dust storm, the TD dust outflow reached the northern slope of TP (36.5°N) with a flux of 6.6 Gg day<sup>-1</sup>, but this outflow flux decreases by half upon arrival at 35.2°N due to dry deposition, which has the potential to change the surface albedo, especially when the land surface is covered by snow or glacier. Dust outflow flux has an obvious diurnal cycle. The southward (from the TD to the TP) dust flow peaked at approximately 16:00 LT (UTC + 6 h) during the event due to diurnal variations of upslope flow driven by day time heating over the TP. In addition, the stronger thermal effect of the TP in the afternoon also leads to stronger convergence circulation, which transported dust from the TD to the TP.

[29] The model simulations show that TD dust has a SW cooling effect with an average value of  $-11.71 \text{ W m}^{-2}$  and a LW warming effect with an average value of  $6.13 \text{ W m}^{-2}$  at the surface over the TP. At the TOA, TD dust has a negative net (LW + SW) radiative forcing of  $-3.97 \text{ W m}^{-2}$  over the TP. In the atmosphere, TD dust can induce SW warming of  $6.69 \text{ W m}^{-2}$ , LW cooling of  $-5.08 \text{ W m}^{-2}$ , and net radiative warming of  $1.61 \text{ W m}^{-2}$  and hence modify the atmospheric heating profiles. The dust-induced SW heating and LW cooling in the atmosphere reduce gradually with altitude. On net effect, TD dust significantly cools the atmosphere near the surface and heats the atmosphere above with a maximum heating rate of  $0.11 \text{ K day}^{-1}$  at about 7 km over the TP during this dust event. Our estimated dust radiative forcing and heating rate over the TP are overall comparable to those estimated near the TD dust source region in the previous studies [Lau et al., 2006; Ge et al., 2011], although the different region, time period, and methods used to calculate radiative forcing may contribute to differences in the results.

[30] Although more extensive measurements, particularly for in situ observations, are needed to further evaluate the simulated transport of TD dust and its radiative forcing over the TP, the WRF-Chem model with a relatively fine resolution well represents the large horizontal gradients of surface elevation and complicated terrain over the dust source and surrounding regions compared with available satellite retrievals and provides confidence for use of this model in regional climate application over the TD and TP. This study indicates that the radiative forcing of dust modified the surface and TOA energy budget and atmospheric heating profile, which may modulate the stability of the atmosphere as well as surface sensible and latent heating and influence the role of the TP as a heat pump. Depending on the frequency of dust intrusion into the TP from the TD to the north and the Thar Desert to the south, dust may have significant implications for the circulation and monsoon climate in Asia. Analysis of synoptic conditions to assess the frequency of occurrence of circulation regimes conducive to dust transport over the TP, as well as performing long-term simulations to estimate dust forcing and impacts in that region, can help quantify the role of dust in the Asian monsoon systems. As dust from the TD is an important contributor to long-range dust transport, characterizing the seasonal emission of dust and its transport by different synoptic

conditions would be important to better assess the influence of TD dust worldwide. In addition, although the indirect radiative effect (dust-cloud interaction) and dust deposition-induced snow-albedo effect of dust are not investigated in this study, we plan to examine them to further understand the regional climate impact of TD dust.

[31] **Acknowledgment.** We acknowledge Cyrille Flamant and two anonymous reviewers for their valuable comments and suggestions. This work was jointly supported by the National Basic Research Program of China (2012CB955301), the Special Scientific Research Project for Public Interest (Grant No. GYHY201206009), the Program for Changjiang Scholars and Innovative Research Team in University (IRT1018), and the Scholarship Award for Excellent Doctoral Student granted by Ministry of Education of China. This research was performed by the first author during her visit to PNNL in collaborations with PNNL scientists, whose research was sponsored by the U.S. Department of Energy’s Office of Science Biological and Environmental Research. PNNL is operated for the U.S. DOE by Battelle Memorial Institute under contract DE-AC06-76RLO1830.

## References

- Barnard, J., J. Fast, G. Paredes-Miranda, W. Arnott, and A. Laskin (2010), Technical note: Evaluation of the WRF-Chem “aerosol chemical to aerosol optical properties” module using data from the MILAGRO campaign, *Atmos. Chem. Phys.*, *10*, 7325–7340, doi:10.5194/acpd-10-8927-2010.
- Chen, F., K. Mitchell, J. Schaake, Y. Xue, H.-L. Pan, V. Koren, Q. Y. Duan, M. Ek, and A. Betts (1996), Modeling of land surface evaporation by four schemes and comparison with FIFE observations, *J. Geophys. Res.*, *101* (D3), 7251–7268, doi:10.1029/95JD02165.
- Chen, F., and J. Dudhia (2001), Coupling an advanced land surface-hydrology model with the Penn State-NCAR MM5 modeling system. Part I: Model implementation and sensitivity, *Mon. Weather Rev.*, *129*, 569–585, doi: [http://dx.doi.org/10.1175/1520-0493\(2001\)129<0569:CAALSH>2.0.CO;2](http://dx.doi.org/10.1175/1520-0493(2001)129<0569:CAALSH>2.0.CO;2); DOI:10.1175/1520-0493(2001)129%3c0569:CAALSH%3e2.0.CO;2.
- Fast, J. D., W. I. Gustafson Jr., R. C. Easter, R. A. Zaveri, J. C. Barnard, E. G. Chapman, G. A. Grell, and S. E. Peckham (2006), Evolution of ozone, particulates, and aerosol direct radiative forcing in the vicinity of Houston using a fully coupled meteorology-chemistry-aerosol model, *J. Geophys. Res.*, *111*, D21305, doi:10.1029/2005JD006721.
- Fast, J., et al. (2009), Evaluating simulated primary anthropogenic and biomass burning organic aerosols during MILAGRO: Implications for assessing treatments of secondary organic aerosols, *Atmos. Chem. Phys.*, *9*, 6191–6215, doi:10.5194/acpd-9-4805-2009.
- Forster, P., et al. (2007), Radiative forcing of climate change, in *Climate Change 2007: The Physical Science Basis. Contribution of Working Group I to the Fourth Assessment Report of the Intergovernmental Panel on Climate Change*, edited by S. Solomon, D. Qin, M. Manning, Z. Chen, M. Marquis, K. B. Averyt, M. Tignor, and H. L. Miller, pp. 129–234, Cambridge Univ. Press, Cambridge, United Kingdom and New York, NY, USA.
- Gautam, R., N. Hsu, K. Lau, and M. Kafatos (2009), Aerosol and rainfall variability over the Indian monsoon region: Distributions, trends and coupling, *Ann. Geophys.*, *27*, 3691–3703, doi:10.5194/angeo-27-3691-2009.
- Ge, J. M., J. Su, T. P. Ackerman, Q. Fu, J. P. Huang, and J. S. Shi (2010), Dust aerosol optical properties retrieval and radiative forcing over northwestern China during the 2008 China-U.S. joint field experiment, *J. Geophys. Res.*, *115*, D00K12, doi:10.1029/2009JD013263.
- Ge, J. M., J. P. Huang, J. Su, J. R. Bi, and Q. Fu (2011), Shortwave radiative closure experiment and direct forcing of dust aerosol over northwestern China, *Geophys. Res. Lett.*, *38*, L24803, doi:10.1029/2011GL049571.
- Ginoux, P., M. Chin, I. Tegen, J. M. Prospero, B. Holben, O. Dubovik, and S. J. Lin (2001), Sources and distributions of dust aerosols simulated with the GOCART model, *J. Geophys. Res.*, *106*, 20255–20220, 20273, doi:10.1029/2000JD000053.
- Grell, G. A., J. Dudhia, D. R. Stauffer, N. C. f. A. R. Mesoscale, and M. M. Dicismon (1994), A description of the fifth-generation Penn State/NCAR mesoscale model (MM5), *NCAR Tech. Note. NCAR/TN-3981STR*, 117 pp.
- Grell, G. A., S. E. Peckham, R. Schmitz, S. A. McKeen, G. Frost, W. C. Skamarock, and B. Eder (2005), Fully coupled “online” chemistry within the WRF model, *Atmos. Environ.*, *39*, 6957–6975, doi:10.1016/j.atmosenv.2005.04.027.
- Hsu, N. C., S. C. Tsay, M. D. King, and J. R. Herman (2006), Deep blue retrievals of Asian aerosol properties during ACE-Asia, *IEEE Trans. Geosci. Remote Sens.*, *44*, 3180–3195, doi:10.1109/TGRS.2006.879540.
- Huang, J., P. Minnis, B. Lin, T. Wang, Y. Yi, Y. Hu, S. Sun-Mack, and K. Ayers (2006a), Possible influences of Asian dust aerosols on cloud

- properties and radiative forcing observed from MODIS and CERES, *Geophys. Res. Lett.*, **33**, L06824, doi:10.1029/2005GL024724.
- Huang, J., B. Lin, P. Minnis, T. Wang, X. Wang, Y. Hu, Y. Yi, and J. K. Ayers (2006b), Satellite-based assessment of possible dust aerosols semi-direct effect on cloud water path over East Asia, *Geophys. Res. Lett.*, **33**, L19802, doi:10.1029/2006GL026561.
- Huang, J., P. Minnis, B. Chen, Z. Huang, Z. Liu, Q. Zhao, Y. Yi, and J. K. Ayers (2008), Long-range transport and vertical structure of Asian dust from CALIPSO and surface measurements during PACDEX, *J. Geophys. Res.*, **113**, D23212, doi:10.1029/2008JD010620.
- Huang, J., P. Minnis, Y. Yi, Q. Tang, X. Wang, Y. Hu, Z. Liu, K. Ayers, C. Trepte, and D. Winker (2007), Summer dust aerosols detected from CALIPSO over the Tibetan Plateau, *Geophys. Res. Lett.*, **34**, L18805, doi:10.1029/2007GL029938, 2007.
- Huang, J., Q. Fu, J. Su, Q. Tang, P. Minnis, Y. Hu, Y. Yi, and Q. Zhao (2009), Taklimakan dust aerosol radiative heating derived from CALIPSO observations using the Fu-Liou radiation model with CERES constraints, *Atmos. Chem. Phys.*, **9**, 4011–4021, doi:10.5194/acp-9-4011-2009.
- Huang, J., I. Minnis, H. Yan, Y. Yi, B. Chen, L. Zhang and J. K. Ayers (2010), Dust aerosol effect on semi-arid climate over Northwest China detected from A-train satellite measurements, *Atmos. Chem. Phys.*, **10**, 6863–6872, doi:10.5194/acp-10-6863-2010.
- Iacono, M. J., E. J. Mlawer, S. A. Clough, and J. J. Morcrette (2000), Impact of an improved longwave radiation model, RRTM, on the energy budget and thermodynamic properties of the NCAR community climate model, CCM3, *J. Geophys. Res.*, **105**, 14, doi:10.1029/2000JD900091.
- Janjic', Z. I. (1994), The step-mountain Eta coordinate model: Further development of the convection, viscous sublayer and turbulent closure schemes, *Mon. Weather Rev.*, **122**, 927–945, doi:10.1175/1520-0493(1994)122<0927:TSMECM>2.0.CO;2.
- Janjic', Z. I. (2001), Nonsingular implementation of the Mellor-Yamada level 2.5 scheme in the NCEP Meso model. NOAA/NWS/ NCEP Office Note 437, 61 pp.
- Kaufman, Y. J., A. E. Wald, L. A. Remer, B. C. Gao, R. R. Li, and L. Flynn (1997), The MODIS 2.1- $\mu\text{m}$  channel-correlation with visible reflectance for use in remote sensing of aerosol, *IEEE Trans. Geosci. Remote Sens.*, **35**, 1286–1298, doi:10.1109/36.628795.
- Koren, I., Y. J. Kaufman, L. A. Remer, and J. V. Martins (2004), Measurement of the effect of Amazon smoke on inhibition of cloud formation, *Science*, **303**, 1342–1345, doi:10.1126/science.1089424.
- Kuhlmann, J., and J. Quaas (2010), How can aerosols affect the Asian summer monsoon? Assessment during three consecutive pre-monsoon seasons from CALIPSO satellite data, *Atmos. Chem. Phys.*, **10**, 4673–4688, doi:10.5194/acp-10-4673-2010.
- Lau, K. M., M. K. Kim, and K. M. Kim (2006), Asian summer monsoon anomalies induced by aerosol direct forcing: The role of the Tibetan Plateau, *Clim. Dyn.*, **26**(7–8), 855–864, doi:10.1007/s00382-006-0114-z.
- Lau, K., K. Kim, Y. Sud, and G. Walker (2009), A GCM study of the response of the atmospheric water cycle of West Africa and the Atlantic to Saharan dust radiative forcing, *Ann. Geophys.*, **27**, 4023–4037, doi:10.5194/angeo-27-4023-2009.
- Lau, W. K. M., M. K. Kim, K. M. Kim, and W. S. Lee (2010), Enhanced surface warming and accelerated snow melt in the Himalayas and Tibetan Plateau induced by absorbing aerosols, *Environ. Res. Lett.*, **5**, 025204, doi:10.1088/1748-9326/5/2/025204.
- Li, Z., et al. (2011), East Asian Studies of Tropospheric Aerosols and their Impact on Regional Climate (EAST-AIRC): An overview, *J. Geophys. Res.*, **116**, D00K34, doi:10.1029/2010JD015257.
- Li, W., and S. Yu (2001), Spatio-temporal characteristics of aerosol distribution over Tibetan Plateau and numerical simulation of radiative forcing and climate response, *Sci. China*, **44**(Supp), 375–384, (in Chinese), doi:10.1007/BF02912009.
- Liu, Y., J. Huang, G. Shi, T. Takamura, P. Khatri, J. Bi, J. Shi, T. Wang, X. Wang, and B. Zhang (2011), Aerosol optical properties and radiative effect determined from sky-radiometer over Loess Plateau of Northwest China, *Atmos. Chem. Phys.*, **11**, 11455–11463, doi:10.5194/acp-11-11455-2011.
- Liu, Z., et al. (2008), Airborne dust distributions over the Tibetan Plateau and surrounding areas derived from the first year of CALIPSO lidar observations, *Atmos. Chem. Phys.*, **8**, 5957–5977, doi:10.5194/acp-8-5045-2008.
- Martonchik, J. V., D. J. Diner, R. A. Kahn, T. P. Ackerman, M. M. Verstraete, B. Pinty, and H. R. Gordon (1998), Techniques for the retrieval of aerosol properties over land and ocean using multiangle imaging, *IEEE Trans. Geosci. Remote Sens.*, **36**, 1212–1227, doi:10.1109/36.701027.
- Martonchik, J. V., D. J. Diner, K. A. Crean, and M. A. Bull (2002), Regional aerosol retrieval results from MISR, *IEEE Trans. Geosci. Remote Sens.*, **40**, 1520–1531, doi:10.1109/TGRS.2002.801142.
- Martonchik, J., D. Diner, R. Kahn, B. Gaitley, and B. Holben (2004), Comparison of MISR and AERONET aerosol optical depths over desert sites, *Geophys. Res. Lett.*, **31**, L16102, doi:10.1029/2004GL019807.
- McKeen, S. A., G. Wotawa, D. D. Parrish, J. S. Holloway, M. P. Buhr, G. Hübler, F. C. Fehsenfeld, and J. F. Meagher (2002), Ozone production from Canadian wildfires during June and July of 1995, *J. Geophys. Res.*, **107**, 4192, doi:10.1029/2001JD000697.
- Mlawer, E. J., S. J. Taubman, P. D. Brown, M. J. Iacono, and S. A. Clough (1997), Radiative transfer for inhomogeneous atmospheres: RRTM, a validated correlated-k model for the longwave, *J. Geophys. Res.*, **102**, 16663–16616, 16682, doi:10.1029/97JD00237.
- Morrison, H., J. Curry, and V. Khvorostyanov (2005), A new double-moment microphysics parameterization for application in cloud and climate models. Part I: Description, *J. Atmos. Sci.*, **62**, 1665–1677, doi:http://dx.doi.org/10.1175/JAS3446.1.
- Murayama, T., et al. (2001), Ground-based network observation of Asian dust events of April 1998 in east Asia, *J. Geophys. Res.*, **106**, 18345–18359, doi:10.1029/2000JD900554.
- Qian, W., Quan, L., and S. Shi (2002), Variations of the dust storm in China and its climatic control, *J. Climate*, **15**, 1216–1229, doi:http://dx.doi.org/10.1175/1520-0442(2002)015<1216:VOTDSI>2.0.CO;2 DOI:10.1175/1520-0442%282002%29015%3C1216:VOTDSI%3E2.0.CO;2.
- Qian, Y., D. Gong, J. Fan, L. R. Leung, R. Bennartz, D. Chen, and W. Wang (2009), Heavy pollution suppresses light rain in China: Observations and modeling, *J. Geophys. Res.*, **114**, D00K02, doi:10.1029/2008JD011575.
- Qian, Y., M. Flanner, L. R. Leung, and W. Wang (2011), Sensitivity studies on the impacts of Tibetan Plateau snowpack pollution on the Asian hydrological cycle and monsoon climate, *Atmos. Chem. Phys.*, **11**, 1929–1948, doi:10.5194/acp-11-1929-2011.
- Qin, D., P. A. Mayewski, C. P. Wake, S. Kang, and J. Ren (2000), Evidence for recent climate change from ice cores in the central Himalayas, *Ann. Glaciol.*, **31**, 153–158.
- Ramanathan, V., P. Crutzen, J. Kiehl, and D. Rosenfeld (2001), Aerosols, climate, and the hydrological cycle, *Science*, **294**, 2119–2124, doi:10.1126/science.1064034.
- Rienecker, M. M., et al. (2011), MERRA: NASA's Modern-Era Retrospective Analysis for Research and Applications, *J. Climate*, **24**, 3624–3648, doi: http://dx.doi.org/10.1175/JCLI-D-11-00015.1.
- Seikiyama, T. T., T. Y. Tanaka, T. Maki, and M. Mikami (2011), The effects of snow cover and soil moisture on Asian dust: II. Emission estimation by lidar data assimilation, *SOLA*, **7**, 40–43, doi:10.2151/sola.7A-011.
- Skamarock, W., et al. (2008), A description of the advanced research WRF version 3, NCAR technical note NCAR/TN/u2013475.
- Shao Y., K. H. Wyrwoli, A. Chappell, J. Huang, Z. Lin, G. H. McTainsh, M. Mikami, T. Y. Tanaka, X. Wang and S. Yoon (2011), Dust cycle: An emerging core theme in Earth system science, *Aeolian Res.*, **2**, 181–204, doi:10.1016/j.aeolia.2011.02.001.
- Stauffer, D. R., and N. L. Seaman (1990), Use of four-dimensional data assimilation in a limited-area mesoscale model. Part I: Experiments with synoptic-scale data, *Mon. Wea. Rev.*, **118**, 1250–1277, doi:http://dx.doi.org/10.1175/1520-0493(1990)118<1250:UOFDDA>2.0.CO;2 DOI:10.1175/1520-0493%281990%29118%3C1250:UOFDDA%3E2.0.CO;2.
- Su, J., J. Huang, Q. Fu, P. Minnis, J. Ge, and J. Bi (2008), Estimation of Asian dust aerosol effect on cloud radiation forcing using Fu-Liou radiative model and CERES measurements, *Atmos. Chem. Phys.*, **8**, 2763–2771, doi:10.5194/acp-8-2763-2008.
- Tao, S., and Y. Ding (1981), Observational evidence of the influence of the Qinghai-Xizang (Tibet) Plateau on the occurrence of heavy rain and severe convective storms in China, *Bull. Am. Meteor. Soc.*, **62**, 23–30, doi:http://dx.doi.org/10.1175/1520-0477(1981)062<0023:OEOTIO>2.0.CO;2 DOI:10.1175/1520-0477(1981)062%3c0023:OEOTIO%3e2.0.CO;2.
- Twomey, S. A., M. Piepgrass, and T. Wolfe (1984), An assessment of the impact of pollution on global cloud albedo, *Tellus B*, **36**, 356–366, doi:10.1111/j.1600-0889.1984.tb00254.x.
- Uno, I., et al. (2004), Numerical study of Asian dust transport during the springtime of 2001 simulated with the Chemical Weather Forecasting System (CFORS) model, *J. Geophys. Res.*, **109**, doi:10.1029/2003JD004222.
- van der Werf, G. R., J. T. Randerson, L. Giglio, G. J. Collatz, M. Mu, P. S. Kasibhatla, D. C. Morton, R. S. DeFries, Y. Jin, and T. T. van Leeuwen (2010), Global fire emissions and the contribution of deforestation, savanna, forest, agricultural, and peat fires (1997–2009), *Atmos. Chem. Phys.*, **10**, 11707–11735, doi:10.5194/acpd-10-16153-2010.
- Vaughan, M., S. Young, D. Winker, K. Powell, A. Omar, Z. Liu, Y. Hu, and C. Hostetler (2004), Fully automated analysis of space-based lidar data: An overview of the CALIPSO retrieval algorithms and data products, *Proc. SPIE*, **5575**, 16–30, doi:10.1117/12.572024.
- Wang, X., J. Huang, M. Ji, and K. Higuchi (2008), Variability of East Asia dust events and their long-term trend, *Atmos. Environ.*, **42**, 3156–3165, doi:10.1016/j.atmosenv.2007.07.046.
- Wang, W., J. Huang, P. Minnis, Y. Hu, J. Li, Z. Huang, J. K. Ayers, and T. Wang (2010), Dusty cloud properties and radiative forcing over dust

- source and downwind regions derived from A-Train data during the Pacific Dust Experiment, *J. Geophys. Res.*, *115*, D00H35, doi:10.1029/2010JD014109.
- Winker, D. M., J. Pelon, and M. P. McCormick (2003), The CALIPSO mission: Spaceborne lidar for observation of aerosols and clouds, *Proc. SPIE*, *4893*, 1–11, doi:10.1117/12.466539.
- Wu, G., and Y. Zhang (1998), Tibetan Plateau forcing and the timing of the monsoon onset over South Asia and the South China Sea, *Mon. Weather Rev.*, *126*, 913–927, doi:10.1175/1520-0493(1998)126<0913:TPFATT.2.0.CO;2.
- Wu, G., Y. Liu, T. Wang, R. Wan, X. Liu, W. Li, Z. Wang, Q. Zhang, A. Duan, and X. Y. Liang (2007), The influence of mechanical and thermal forcing by the Tibetan Plateau on Asian climate, *J. Hydrometeorol.*, *8*, 770–789, doi:10.1175/JHM609.1.
- Xia, X., P. Wang, Y. Wang, Z. Li, J. Xin, J. Liu, and H. Chen (2008), Aerosol optical depth over the Tibetan Plateau and its relation to aerosols over the Taklimakan Desert, *Geophys. Res. Lett.*, *35*, L16804, doi:10.1029/2008GL034981.
- Xu, J., S. Hou, D. Qin, S. Kang, J. Ren, and J. Ming (2007), Dust storm activity over the Tibetan Plateau recorded by a shallow ice core from the north slope of Mt. Qomolangma (Everest), Tibet-Himal region, *Geophys. Res. Lett.*, *34*, L17504, doi:10.1029/2007GL030853.
- Yanai, M., and C. Li (1994), Mechanism of heating and the boundary layer over the Tibetan Plateau, *Mon. Wea. Rev.*, *122*, 305–323, doi:http://dx.doi.org/10.1175/1520-0493(1994)122<0305:MOHATB>2.0.CO;2.
- Yang, K., T. Koike, H. Fujii, T. Tamura, X. Xu, L. Bian, and M. Zhou (2004), The daytime evolution of the atmospheric boundary layer and convection over the Tibetan Plateau: Observations and simulations, *J. Meteor. Soc. Jpn.*, *6*, 1777–1792, doi:10.2151/jmsj.82.1777.
- Ye, D. Z., and G. X. Wu (1998), The role of the heat source of the Tibetan Plateau in the general circulation, *Meteorol. Atmos. Phys.*, *67*, 181–198, doi:10.1007/BF01277509.
- Yumimoto, K., K. Eguchi, I. Uno, T. Takemura, Z. Liu, A. Shimizu, and N. Sugimoto (2009), An elevated large-scale dust veil from the Taklimakan Desert: Intercontinental transport and three-dimensional structure as captured by CALIPSO and regional and global models, *Atmos. Chem. Phys.*, *9*, 8545–8558, doi:10.5194/acp-9-8545-2009.
- Yumimoto, K., K. Eguchi, I. Uno, T. Takemura, Z. Liu, A. Shimizu, N. Sugimoto, and K. Strawbridge (2010), Summertime trans-Pacific transport of Asian dust, *Geophys. Res. Lett.*, *37*, L18815, doi:10.1029/2010GL043995.
- Zaveri, R. A., and L. K. Peters (1999), A new lumped structure photochemical mechanism for large-scale applications, *J. Geophys. Res.*, *104*, 30387–30330,30415, doi:10.1029/1999JD900876.
- Zaveri, R. A., R. C. Easter, J. D. Fast, and L. K. Peters (2008), Model for simulating aerosol interactions and chemistry (MOSAIC), *J. Geophys. Res.*, *113*, D13204, doi:10.1029/2007JD008782.
- Zhang, X., A. Richard, J. J. Cao, Z. S. An, and D. Wang (2001), Atmospheric dust aerosol over the Tibetan Plateau, *J. Geophys. Res.*, *106*, D16, doi:10.1029/2000JD900672.
- Zhang, Y., M. Takahashi, and L. Guo (2008), Analysis of the East Asian subtropical westerly jet simulated by CCSR/NIES/FRCGC coupled climate system model, *J. Meteor. Soc. Jpn.*, *86*, 257–278, doi:10.2151/jmsj.86.257.
- Zhao, C., X. Liu, L. R. Leung, B. Johnson, S. McFarlane, W. Gustafson Jr., J. Fast, and R. Easter (2010), The spatial distribution of mineral dust and its shortwave radiative forcing over North Africa: Modeling sensitivities to dust emissions and aerosol size treatments, *Atmos. Chem. Phys.*, *10*, 8821–8838, doi:10.5194/acp-10-8821-2010.
- Zhao, C., X. Liu, L. R. Leung, and S. Hagos (2011), Radiative impact of mineral dust on monsoon precipitation variability over West Africa, *Atmos. Chem. Phys.*, *11*, 1879–1893, doi:10.5194/acp-11-1879-2011.
- Zhao, C., X. Liu, and L. R. Leung (2012), Impact of the Desert dust on the summer monsoon system over Southwestern North America, *Atmos. Chem. Phys.*, *12*, 3717–3731, doi:10.5194/acp-12-3717-2012.